Lucky imaging and aperture synthesis with low-redundancy apertures

Jennifer E. Ward,[1] William T. Rhodes,[2] and John T. Sheridan[1,*]

[1]School of Electrical, Electronic and Mechanical Engineering, Optoelectronic Research Centre, SFI-Strategic Research Cluster in Solar Energy Conversion, College of Engineering, Mathematics and Physical Sciences, University College Dublin, Belfield, Dublin 4, Ireland

[2]Imaging Technology Center and Department of Electrical Engineering, Florida Atlantic University, Boca Raton, Florida 33431, USA

*Corresponding author: john.sheridan@ucd.ie

Received 9 June 2008; revised 29 September 2008; accepted 30 September 2008; posted 2 October 2008 (Doc. ID 97181); published 19 November 2008

Lucky imaging, used with some success in astronomical and even horizontal-path imaging, relies on fleeting conditions of the atmosphere that allow momentary improvements in image quality, at least in portions of an image. Aperture synthesis allows a larger aperture and, thus, a higher-resolution imaging system to be synthesized through the superposition of image spatial-frequency components gathered by cooperative combinations of smaller subapertures. A combination of lucky imaging and aperture synthesis strengthens both methods for obtaining improved images through the turbulent atmosphere. We realize the lucky imaging condition appropriate for aperture synthesis imaging for a pair of rectangular subapertures and demonstrate that this condition occurs when the signal energy associated with bandpass spatial-frequency components achieves its maximum value.

OCIS codes: 110.0115, 100.3175.

1. Introduction

Aperture synthesis has been investigated for decades as a means of achieving high-resolution telescope imagery with smaller apertures acting cooperatively [1–6]. The basic concept is illustrated in Fig. 1. As shown in Figs. 1(a) and 1(b), a two-opening aperture has an associated optical transfer function (OTF) that allows the recording of an image containing both low-pass and bandpass spatial-frequency components, the latter occupying a frequency band that depends on the spacing between the subapertures. By recording multiple images, obtained with different subaperture spacings, one can add together, in a series of computer operations employing the discrete Fourier transform, 2-D Fourier components that span a large range of spatial frequencies. These operations allow one to effectively synthesize a much larger aperture, as suggested by the cross-section OTFs of Figs. 1(c) and 1(d).

Several methods have been proposed that make possible a significant reduction of the effects of atmospheric turbulence on synthetic-aperture imaging [7–9]. In this paper we introduce a technique, which we believe to be superior, that combines aperture synthesis with lucky imaging.

Lucky imaging relies on recording a snapshot image when the atmosphere is in a "lucky" momentary state of turbulence that does little to degrade at least parts of the image [10,11]. Lucky imaging techniques have been applied with significant success to astronomical imaging [11,12] and with somewhat less success to horizontal path imaging [13,14]. Horizontal-path imaging is especially problematic because the turbulence-induced aberrations are strongly space-variant, or nonisoplanatic. Even for vertical-path imaging, the isoplanatic condition is rarely satisfied for sky objects subtending more than a few arc seconds (Chap. 6 of [5]).

0003-6935/09/010A63-08$15.00/0

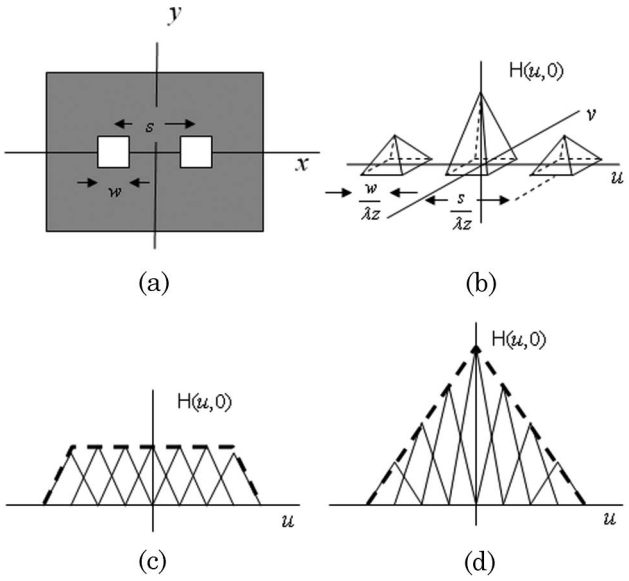

Fig. 1. Illustration of aperture synthesis concept: (a) pupil-plane mask containing two square openings, (b) associated OTF, (c) u axis cross section of large-bandwidth OTF $\mathsf{H}(u,v)$ synthesized by an equal-weighting sum of individual OTF spatial-frequency passbands, (d) same but with weighting appropriate for a conventional OTF. In (c) and (d) the synthesized OTF is denoted by the dashed lines.

The method described in this paper relies on the identification of lucky imaging conditions that make the synthesis of larger effective apertures more easily achieved, with a subsequent improvement in system sensitivity. The scheme requires that the subapertures employed in the synthesis satisfy a low-redundancy condition under which, for a reasonable fraction of the time, the turbulence-induced aberration phases associated with each of the subapertures are well-approximated by piston and tip–tilt only. The reasoning underlying this requirement is made clear in Section 2. Lucky imaging occurs in this context when the wavefront tip–tilt associated with one subaperture is the same, or nearly the same, as that associated with the other.

The method we propose is introduced qualitatively in Section 2, with a more detailed mathematical analysis following in Section 3. Some illustrative numerical simulations are presented in Section 4, and discussion and concluding remarks are presented in Section 5.

2. Basic Concept

By way of specific example we consider the synthesis of a large aperture by means of the 2-D equivalent of the operation illustrated in Fig. 1(c) using a two-square-subaperture mask. Spatial-frequency passband information is obtained from a sequence of images, each image being recorded with a different center-to-center spacing between the subapertures in both the x and y directions. In the absence of turbulence-induced phase aberrations, the resulting synthesized OTF has the appearance of a table top covered by a tablecloth that is flared out at the sides.

The individual exposures are assumed to be sufficiently short that each image corresponds to a particular frozen state of the turbulence. We can represent the momentary phase across a given subaperture by a Taylor series:

$$\phi(x,y) = \phi_o + \alpha_1 x + \beta_1 y + \alpha_2 x^2 + \beta_2 y^2 + \gamma_2 xy + \ldots. \tag{1}$$

If the subapertures are sufficiently small, $\phi(x,y)$ is well approximated by piston phase ϕ_o alone, and the phase of the passband components recorded with a particular subaperture pair is in error by a constant phase difference of the form $\Delta\phi_{ij} = \phi_i - \phi_j$. Since there is substantial overlap between the spatial-frequency passbands contributing to the synthesis —toward the interior of the OTF four nearest-neighbor passbands, positioned at 12:00, 3:00, 6:00, and 9:00 on the clock, overlap by 50%, another four by 25%—it is a relatively simple matter to compare spatial-frequency components known to have the correct phase with overlapping spatial-frequency components in error by unknown phase $\Delta\phi_{ij}$ and make appropriate corrections. One could begin, for example, with the low-frequency image recorded with a single square opening and work outward from there to higher spatial frequencies. The problem with this scheme is that the subapertures must be fairly small, and they are thus unable to collect sufficient light for the short-exposure imaging of faint objects. If the subapertures are made larger, to the point that the phase across an aperture is well approximated by the constant and linear terms of Eq. (1), continuity-of-phase processing can still be easily applied, and the subapertures can be significantly larger. Processing of this kind was demonstrated with some success by Rhodes in 1974 [9].

Nevertheless, despite the improved light-collecting ability of the larger subapertures, the system will still be light-starved for many objects of interest. Fortunately, lucky imaging conditions make possible the imaging of even dimmer objects by allowing the subapertures to be larger still, while virtually guaranteeing that images selected for the synthesis operation satisfy the linear aberration phase, i.e., tilt–tip, approximation condition. The desired lucky imaging condition is determined through a measure of the image signal energy E in the spatial-frequency passband of concern, i.e., within the boundaries of the passband(s) in Fig. 1(b). This quantity can be expressed in the form of the integral

$$\mathsf{E} = \int_{v_l}^{v_u}\int_{u_l}^{u_u} |\hat{I}(u,v)|^2 \mathrm{d}u\,\mathrm{d}v, \tag{2}$$

where $|\hat{I}(u,v)|^2$ is the energy spectrum of the image intensity distribution and where u_l, u_u, v_l, and v_u denote the lower and upper spatial-frequency limits to the passband. The value of this integral will vary from image to image. In our synthesis we wish to

identify and use the image(s) for which the value of E is largest, hoping that this value is quite close to the maximum value possible.

Indeed, as we establish analytically in Section 3, when this bandpass signal energy attains its maximum possible value for a given object, then (a) the wavefront phase aberrations across the two subapertures contain no significant Taylor series components beyond first order, (b) the tip–tilt parameters for the two subapertures are the same, and (c) the modulus of the bandpass portion of the OTF is of the desired 2-D triangular form, such as is illustrated in Fig. 1(b) for the aberration-free case. These three conditions together greatly facilitate the aperture synthesis operation.

The basic aperture synthesis with lucky imaging operation proceeds as follows:

i. A reference low-frequency image is recorded to use as a starting point for the synthesis process. This image should be selected from an ensemble of images made of the (non-time-varying) object using a pupil-plane mask that consists of a single square subaperture. The selection should be governed by conventional lucky imaging principles, i.e., the image should be selected for its good contrast and absence of apparent aberrations. Since the subapertures are, by choice, sufficiently small that the turbulence-induced phase aberrations are more likely to be limited to piston plus tip–tilt, many good candidate low-frequency images should be available.

ii. A sequence of a suitably large number of images is then recorded with a particular small-spacing two-subaperture mask in the pupil plane.

iii. Each image in this sequence is Fourier transformed and the signal energy in the passband of concern is measured in accord with Eq. (2).

iv. The passband components are extracted from that image from the sequence that contains the greatest passband signal energy. These components are then added after they have been corrected by means of overlap-region comparisons for the piston and tip–tilt phase errors.

v. The process is continued as in (i)–(iv) with masks containing more widely spaced subapertures. Each new set of phase-corrected passband components is added to the existing collection, until the entire range of spatial-frequency components has been brought together in one large-bandwidth image. Residual errors arise only because selection of the lucky images is governed by statistics, and there is no guarantee that the images selected for the synthesis operation actually contain the maximum achievable value of energy E. The effective OTF that results from this procedure can be adjusted as desired, in a manner such as that suggested by Fig. 1(d).

3. Supporting Analysis

The effectiveness of the procedure just described depends on the validity of the claims made, in relation to Eq. (2), regarding the nature of the optimum lucky bandpass image. These claims are established in this section by means of an analysis of the magnitude and phase of the two-subaperture OTF. In general, the OTF associated with the imaging of spatially incoherent, quasi-monochromatic objects is given by Goodman [15]:

$$\mathsf{H}(u,v) = \left.\frac{p(x,y) \otimes\otimes p(x,y)}{\mathrm{NF}}\right|_{\substack{x=\lambda z u \\ y=\lambda z v}}, \tag{3}$$

where $p(x,y)$ is the pupil function referred to the exit pupil, $\otimes\otimes$ denotes a 2-D correlation, λ is the wavelength, z is the distance from the exit pupil to the image plane, and normalizing factor NF is selected such that $\mathsf{H}(0,0) = 1$. The pupil function of interest to us is modeled by

$$p(x,y) = p_1(x,y) ** \delta(x + s/2, y) + p_2(x,y) ** \delta(x - s/2, y), \tag{4}$$

where

$$p_i(x,y) = \mathrm{rect}(x/w, y/w) e^{j\phi_i} e^{j2\pi(\alpha_i x + \beta_i y)}, \tag{5}$$

$i = 1, 2$, and $\mathrm{rect}(x,y)$ denotes the unit rectangle function. Note that the aberration phase is limited to piston plus tip–tilt, a point discussed later in this section. Exploiting properties of correlation and convolution easily established in the Fourier domain we can write, in shorthand notation,

$$\begin{aligned} p \otimes\otimes p &= (p_1 ** \delta_{+1} + p_2 ** \delta_{-1}) \otimes \\ &\otimes (p_1 ** \delta_{+1} + p_2 ** \delta_{-1}) = p_1 \otimes\otimes p_1 + p_2 \otimes \\ &\otimes p_2 + (p_1 \otimes\otimes p_2) ** \delta_{+2} + (p_2 \otimes\otimes p_1) ** \delta_{-2}, \end{aligned} \tag{6}$$

where $**$ denotes a 2-D convolution and $\delta_{\pm n} = \delta(x \pm ns/2, y)$. From Eq. (6) we see that the basic functions of interest to us are the auto- and cross-correlations of $p_1(x,y)$ and $p_2(x,y)$. These are shown in Appendix A to be given by

$$\begin{aligned} p_m(x,y) \otimes\otimes p_n(x,y) &= \mathrm{tri}\left(\frac{x}{w}, \frac{y}{w}\right) \\ &\times \mathrm{sinc}[\Delta\alpha_{nm}(w - |x|),\ \Delta\beta_{nm}(w - |y|)] \\ &\times e^{j\Delta\phi_{mn}} e^{j2\pi(\bar{\alpha}x + \bar{\beta}y)}, \end{aligned} \tag{7}$$

$$p_m(x,y) \otimes\otimes p_m(x,y) = \mathrm{tri}\left(\frac{x}{w}, \frac{y}{w}\right) e^{j2\pi(\alpha_m x + \beta_m y)}, \tag{8}$$

respectively, where $\mathrm{tri}(x)$ is the unit triangle function (unit height, unit area), $\mathrm{sinc}(x) = (1/\pi x)\sin \pi x$,

$\Delta\phi_{ij} = \phi_i - \phi_j$, $\Delta\alpha_{ij} = \alpha_i - \alpha_j$, and $\bar{\alpha} = (\alpha_i + \alpha_j)/2$. Both functions have been normalized to unity at the origin. From Eq. (8) we can obtain an expression for the low-frequency portion of the OTF (again normalized to unity at the peak):

$$\begin{aligned} & p_1 \otimes\otimes\, p_1 + p_2 \otimes\otimes\, p_2 \\ & = \mathrm{tri}\left(\frac{x}{w}, \frac{y}{w}\right) \times \left[e^{j2\pi(\alpha_1 x + \beta_1 y)} + e^{j2\pi(\alpha_1 x + \beta_1 y)}\right] \\ & = \mathrm{tri}\left(\frac{x}{w}, \frac{y}{w}\right) \times \cos\left[2\pi(\Delta\alpha_{12} x + \Delta\beta_{12} y)\right] e^{j2\pi(\bar{\alpha}x + \bar{\beta}y)}. \end{aligned} \tag{9}$$

These equations have been used in the calculation of the MTF cross sections illustrated in Fig. 2, which shows the effect of differential wavefront tilt, as quantified by $\Delta\alpha_{12} = \alpha_1 - \alpha_2$.

Although by using Eq. (6) and making the substitutions $x = \lambda z u$ and $y = \lambda z v$ we can convert Eqs. (7) and (8) to the forms ultimately needed for the OTF expression in Eq. (3), it is simpler to keep the two equations as they appear above. Equation (7) informs us of the behavior of the bandpass portion of the OTF, the portion that is of particular interest if our objective is to form an image by means of a combination of lucky imaging and aperture synthesis techniques. Note that if the wavefront tip–tilts are identical, $\Delta\alpha_{nm} = \Delta\beta_{nm} = 0$, and the sinc function attains its maximum value of unity, the result satisfies our "lucky" condition. This condition is sensed by means of a Fourier-domain analysis of the image itself. Simply stated, if the image contains any spatial-frequency content within the passband, the energy of that content will achieve its maximum possible value when the wavefront tilts are identical and the modulation transfer function (MTF) achieves its maximum value, as proved in Appendix B. This condition is achieved in a statistical sense through selection of the image that maximizes the value of the integral of Eq. (2). Under these conditions, the passband portion of the OTF is governed by

$$\text{OTF passband}: \quad \mathrm{tri}\left(\frac{x}{w}, \frac{y}{w}\right) e^{j\Delta\phi_{mn}} e^{j2\pi(\alpha x + \beta y)}, \tag{10}$$

while the low-pass portion of the OTF is governed by

$$\text{OTF low pass}: \quad \mathrm{tri}\left(\frac{x}{w}, \frac{y}{w}\right) e^{j2\pi(\alpha x + \beta y)}. \tag{11}$$

The sinc function in Eq. (7) attains a null at the center of the triangle function when $\Delta\alpha_{mn} = 1/w$ or $\Delta\beta_{mn} = 1/w$, in wave-optics terms when the difference in wavefront tilt in either direction equals one full wave across the subapertures. This condition corresponds to a translation of the imaging system point spread function through one Rayleigh-resolution distance. For larger tilts, it is possible to observe multiple nulls introduced by the sinc function in the passband, as illustrated in Fig. 2(d). The numerically processed images shown in Fig. 3 illustrate some of these observations. In these cases the aberration phases were calculated using the Zernike-polynomial-based method described by Roddier [16], a point further discussed in Section 4.

The above analysis began with the assumption that the phase aberrations are always well approximated by piston and tip–tilt alone. This condition will not, in general, be satisfied, and indeed, since we want to use larger subapertures in order to gather more light, we are acting so as to make this assumption less valid. Fortunately this assumption is in fact not required. The results expressed in Eqs. (10) and (11) are in all cases achieved when the specified lucky imaging condition is satisfied. That this is so can be established through an application of Schwarz's inequality, as presented in Appendix B. In the general case of an arbitrary OTF, the MTF associated with an imaging system can only get worse when aberration phases are taken into account [17].

Stated succinctly for our case: maximization of the bandpass energy represented by Eq. (2) is achieved if and only if

a. the subaperture phase functions consist solely of piston and tip–tilt, and
b. the tip–tilt parameters describing the linear phase across the two subapertures are the same.

In this special case the procedure described in Section 2 will still work, although the probability of obtaining a lucky image with nearly maximized bandpass energy decreases as the subaperture size

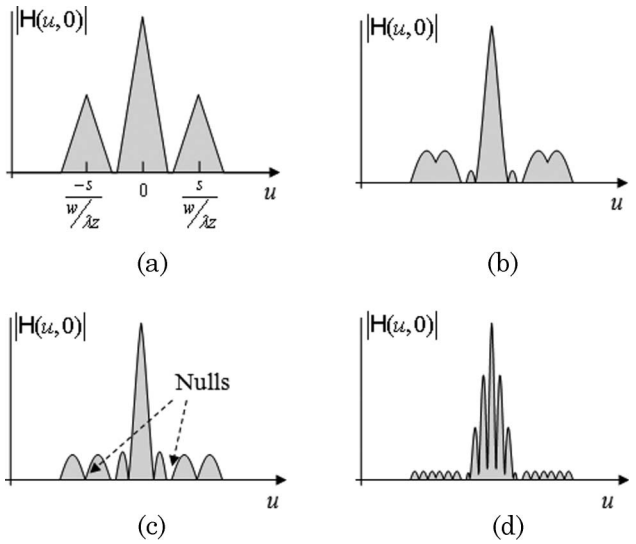

Fig. 2. Cross sections of the modulus of the OTF, $|H(u,0)|$, for different values of the subaperture differential wavefront tilt parameter $\Delta\alpha_{12}$, assuming that $\Delta\beta_{12} = 0$: (a) $\Delta\alpha_{12} = 0$, (b) approximately 1/3 wave differential tilt across the subapertures, (c) one full wave of differential tilt, (d) several waves of differential tilt. Note that the dimples appearing in the passbands in (b) have become full nulls in (c).

Fig. 3. Numerically processed images showing effects of pupil-plane mask and turbulence: (a) original image, (b) image obtained with two-square-opening aperture, no turbulence, (c) same but with turbulence, (d) "lucky" two-subaperture image. Note in (c) the doubling effect on low-frequency components brought about by significant differential aberration phase tilt.

is made larger. Our lucky imaging condition thus becomes the following: "Optimal lucky imaging is experienced when the image passband energy reaches its maximum possible value. In this case the aberration phase consists solely of piston and tip–tilt across the two subapertures and the tilts are the same, i.e., higher-order aberration phase terms are truly negligible."

Under such lucky conditions, we still do not know what the piston and tip–tilt errors are, but we do know that the passband MTF is triangular and that the residual aberration phase is limited to piston plus tip–tilt, i.e., there are no higher-order aberration terms. As suggested earlier, this latter condition makes an aperture-synthesis stitching together of lucky image information much easier, for it is only

necessary to compare overlap data from different lucky images in such a way as to obtain three equations in three unknowns, piston, tip, and tilt [9].

4. Simulations on a Test Image

In this section, to support the analysis presented above, we numerically examine the degradation of a test image "Boat" [18], due to [Fig.3(a)] the presence of a two-square-subaperture mask in the pupil plane of an optical system and to [Fig. 3(b)] the effect of a phase mask that simulates stationary atmospheric turbulence. All the images presented have been normalized, and in all cases a subsection is viewed, located in the range $(50 \rightarrow 462) \times (50 \rightarrow 512)$ pixels within the 512×512 pixel image. (This is done so that, as in a real imaging system, a linear phase tilt in the pupil plane produces a translation of the scene across the viewing plane, as compared to the wrap-around caused by the use of the discrete Fourier transform in the numerical simulations.)

Figure 3(a) was chosen because it contains a wide range of spatial-frequency components. We note that the masts of the boat provide high spatial-frequency content in the image, whereas the foreground contains relatively lower spatial frequencies. The subaperture widths and separations used in the generation of Figs. 3(b)–3(d) are identical to those used to produce Fig. 2.

Figure 3(b) shows the degradation of the image due to the presence of a two-square-subaperture mask in the pupil plane. Figure 3(b) was produced by multiplying the Fourier transform of the image with the OTF of the mask and then inverse Fourier transforming the result. Neither atmospheric turbulence nor noise has been introduced in the calculation of this image. Image resolution is reduced through the OTF.

Figure 3(c) shows the same boat image, but this time the resolution is degraded by the presence of a two-square-subaperture mask *and* a phase aberration function in the pupil plane. The phase aberrations were calculated using a 14-term Zernike polynomial-based expansion following Roddier [16] and do not satisfy lucky conditions. The phase structure function (Chap. 6 of [5]), which in this case defines the mean square difference of the phases incident on the two subapertures, is $0.146\,\mathrm{rad}^2$. Figure 3(c) was obtained by multiplying the two-square-subaperture mask by a phase aberration function, calculating the resulting OTF, multiplying this OTF by the Fourier transform of the original image, and inverse Fourier transforming the result. Two shifted versions of the boat image can be observed in Fig. 3(c), the result of the tip–tilt parameters associated with the two subapertures being different.

Figure 3(d) shows the degradation of the boat image by the presence of a two-square-subaperture mask and a phase aberration function in the pupil plane as in Fig. 3(c). However, in this case, the phase error satisfies the lucky imaging condition, i.e., $\alpha_1 = \alpha_2 = 28$, $\beta_1 = \beta_2 = 0$, and there are no higher-order aberrations. As expected, an improvement in resolution, as compared to Fig. 3(c), is observed. We note that, although the resolution is the same as in Fig. 3(b) (no phase errors), a shift of the boat image can still be observed. This condition indicates that a tilt phase error is indeed present. The passband information associated with Fig. 3(d) constitutes one piece of the spatial-frequency spectrum that would contribute to the final reconstructured image, as described by step (iv) in Section 2.

5. Discussion and Concluding Remarks

The scheme presented above, or a variation of it, offers a means of improving the performance of both conventional optical aperture synthesis and lucky imaging through a combination of the two. It is only suited for imaging non-time-varying objects, and the application of the technique is likely limited to the imaging of astronomical targets with ground based telescopes. The general conclusion of the paper can be stated as follows: Aperture synthesis imaging can be improved by relaxing the nonredundancy condition that is usually required and incorporating lucky imaging, as defined by this paper, to ensure that residual errors can be corrected. A similar conclusion, which supports this view, is reached in another paper appearing in this feature [19]. It should be emphasized that the conditions that determine when lucky imaging has occurred for this scheme are established not in the space domain, as is the usual case, but in the spatial-frequency domain.

It should be noted that the effects of scintillation on the scheme have been ignored. Indeed, if scintillation introduces differences in the amount of light reaching the two subapertures, it will be more difficult to determine when the optimum lucky imaging condition has occurred. The absence of an isoplanatic condition has also been ignored. If, as will generally be true, the isoplanatic patch is smaller than the full image, the method described can in concept be applied to subregions of the image, each sub-region being the size of the isoplanatic patch. Such patch-by-patch synthesis has not, to our knowledge, been successfully implemented so far.

Much remains to be done in a study of the many trade-offs associated with the implementation of the proposed technique. There is a trade-off for example between the size of subapertures used (and, therefore, the light-collecting abilities of the system) and the probability of capturing a lucky image. The strength and scale of the turbulence must also be included in the analysis in order to define the number of images required to obtain a lucky image for a particular optical system. The effects of noise, not examined in this paper, likely present the critical factor in determining the performance of the scheme. In addition, the effect of extending the analysis to the nonnarrowband case assumed must be studied. We note in passing that the image acquisition process can be speeded up, albeit with an attendant reduction in contrast for the bandpass image components,

through the use of pupil-plane masks that contain more than two non-redundantly-spaced subapertures, such as those described in [8].

Appendix A

We desire to calculate the 1-D cross-correlation

$$p_m(x) \otimes p_n(x) = \left[\mathrm{rect}\left(\frac{x}{w}\right) e^{j\frac{\phi_m}{2}} e^{j2\pi\alpha_m x}\right] \otimes \left[\mathrm{rect}\left(\frac{y}{w}\right) e^{j\frac{\phi_n}{2}} e^{j2\pi\alpha_n x}\right]. \tag{A1}$$

For $|x| > w$ the cross-correlation evaluates to zero. For $0 < x < w$, with the aid of Fig. 1(a), we can write Eq. (A1) in the form

$$\begin{aligned} p_m(x) \otimes p_n(x) &= e^{j\frac{\Delta\phi_{mn}}{2}} \int_{x-\frac{w}{2}}^{\frac{w}{2}} e^{j2\pi\alpha_m\xi} e^{-j2\pi\alpha_n(\xi-x)} \mathrm{d}\xi \\ &= e^{j\frac{\Delta\phi_{mn}}{2}} e^{j2\pi\alpha_n x} \int_{x-\frac{w}{2}}^{\frac{w}{2}} e^{-j2\pi(\alpha_n-\alpha_m)\xi} \mathrm{d}\xi \\ &= e^{j\frac{\Delta\phi_{mn}}{2}} e^{j2\pi\alpha_n x} \int_{-\infty}^{\infty} \mathrm{rect}\left(\frac{\xi - \frac{x}{2}}{w-x}\right) e^{-j2\pi(\alpha_n-\alpha_m)\xi} \mathrm{d}\xi, \end{aligned} \tag{A2}$$

where $\Delta\phi_{12} = \phi_1 - \phi_2$. Recognizing the integral as yielding, as a function of $(\alpha_n - \alpha_m)$, the Fourier transform of a shifted and scaled unit rectangle function, we obtain, for $0 < x < w$,

$$p_m(x) \otimes p_n(x) = e^{j\frac{\Delta\phi_{mn}}{2}} e^{j2\pi\alpha_n x}(w-x) \times \mathrm{sinc}[(w-x)(\alpha_n - \alpha_m)] e^{-j2\pi(x/2)(\alpha_n-\alpha_m)}. \tag{A3}$$

Similar results are obtained for $-w < x < 0$. With some manipulation we can then write the 1-D cross-correlation for both positive and negative x in the form

$$p_m(x) \otimes p_n(x) = w\mathrm{tri}\left(\frac{x}{w}\right) \times \mathrm{sinc}[(w-|x|)\Delta\alpha_{nm}] e^{j\frac{\Delta\phi_{mn}}{2}} e^{j2\pi\bar{\alpha}x}, \tag{A4}$$

where $\mathrm{tri}(x)$ is the unit triangle function (unit height, unit area), $\mathrm{sinc}(x) = (1/\pi x)\sin\pi x$, $\Delta\alpha_{21} = \alpha_2 - \alpha_1$, and $\bar{\alpha} = (\alpha_1 + \alpha_2)/2$. Setting n equal to m we obtain the autocorrelation:

$$p_m(x) \otimes p_m(x) = w\mathrm{tri}\left(\frac{x}{w}\right) e^{j2\pi\alpha_m x}. \tag{A5}$$

Equations (7) and (8) easily follow.

Appendix B

Starting with Eq. (A1), but assuming higher order phase terms (aberrations),

$$\begin{aligned} &|p_m \otimes p_n|^2 \\ &= \left| \int_{-\infty}^{+\infty} \left[\mathrm{rect}\left(\frac{\xi}{w}\right) \exp\left(j\frac{\phi_m}{2}\right) \exp\left(j2\pi \sum_{i=1}^{N} \alpha_m(i)\xi^i\right)\right] \right. \\ &\times \left[\mathrm{rect}\left(\frac{(\xi-x)}{w}\right) \exp\left(-j\frac{\phi_n}{2}\right) \right. \\ &\left.\left. \times \exp\left(-j2\pi \sum_{i=1}^{N} \alpha_n(i)(\xi-x)^i\right)\right] \mathrm{d}\xi \right|^2. \end{aligned} \tag{B1}$$

Applying Schwarz's inequality,

$$\begin{aligned} &|p_m \otimes p_n|^2 \\ &\le \int_{-\infty}^{+\infty} \left| \left[\mathrm{rect}\left(\frac{\xi}{w}\right) \exp\left(j\frac{\phi_m}{2}\right) \exp\left(j2\pi \sum_{i=1}^{N} \alpha_m(i)\xi^i\right)\right] \right|^2 \mathrm{d}\xi \\ &\times \int_{-\infty}^{+\infty} \left| \left[\mathrm{rect}\left(\frac{(\xi-x)}{w}\right) \exp\left(-j\frac{\phi_n}{2}\right) \right. \right. \\ &\left.\left. \exp\left(-j2\pi \sum_{i=1}^{N} \alpha_n(i)(\xi-x)^i\right)\right] \right|^2 \mathrm{d}\xi. \end{aligned} \tag{B2}$$

Therefore

$$\begin{aligned} &|p_m \otimes p_n|^2 \\ &\le \int_{-\infty}^{+\infty} \left|\mathrm{rect}\left(\frac{\xi}{w}\right)\right|^2 \mathrm{d}\xi \times \int_{-\infty}^{+\infty} \left|\mathrm{rect}\left(\frac{(\xi-x)}{w}\right)\right|^2 \mathrm{d}\xi = w^2. \end{aligned} \tag{B3}$$

The equality is true only when the $N = 1$ term is nonnegligible and $\exp(j2\pi\alpha_m(1)\xi) \times \exp(-j2\pi\alpha_n(1)\xi) = 1$, which in turn is true only if

$$\alpha_m(1) - \alpha_n(1) = 0 \Rightarrow \alpha_m(1) = \alpha_n(1). \tag{B4}$$

If the $N > 1$ terms are not negligible (i.e., if significant higher order aberrations exist), then it is impossible for the phase expressions to cancel because it would be necessary that

$$\alpha_m(i)\xi^i - \alpha_n(i)(\xi-x)^i = 0. \tag{B5}$$

This cannot be made true for all x values. Therefore higher order aberrations always result in a decrease in the OTF sidelobe values.

Portions of this research were conducted while J. Ward was supported by the FÁS bursary program, as a visiting researcher at Florida Atlantic University. J. Ward and J.T. Sheridan acknowledge the support of Enterprise Ireland (EI) and Science Foun-

dation Ireland (SFI) through the Research Innovation and Proof of Concept Funds, and the Basic Research and Research Frontiers Programs.

References

1. "Woods Hole summer study 1968: synthetic-aperture optics," in *Proceedings of the August 1967 Woods Hole Summer Study* (U.S. National Academy of Sciences, 1968), Vols. I and II.
2. G. W. Stroke, "Optical aperture synthesis using successive exposure of a single photograph and spatial filtering "low-frequency redundancy" suppression," Phys. Lett. A **30**, 485–486 (1969).
3. M. Ryle, A. Hewish, and J. R. Shakeshaft, "The synthesis of large radio telescopes by the use of radio interferometers," IRE Trans. Antennas Propag. **7**, 120–124 (1959).
4. M. Ryle, "A new radio interferometer and its application to the observation of weak radio stars," Proc. R. Soc. London. Ser. A **211**, 351–375 (1952).
5. A. Labeyrie, S. G. Lipson, and P. Nisenson, *An Introduction to Optical Stellar Interferometry* (Cambridge University Press, 2006), Chaps. 5 and 6.
6. P. G. Tuthill, J. D. Monnier, W. C. Danchi, E. H. Wishnow, and C. A Haniff, "Michelson interferometry with the Keck I telescope," Publ. Astron. Soc. Pac. **112** (770), 555–565 (2000).
7. D. H. Rogstad, "A technique for measuring visibility phase with an optical interferometer in the presence of atmospheric seeing," Appl. Opt. **7**, 585–588 (1968).
8. W. T. Rhodes and J. W. Goodman, "Interferometric technique for recording and restoring images degraded by unknown aberrations," J. Opt. Soc. Am. **63**, 647–657 (1973).
9. W. T. Rhodes, "Digital processing of synthetic aperture optical imagery," Opt. Eng. **13**, 267–274 (1974).
10. D. L. Fried, "Probability of getting a lucky short-exposure image through turbulence," J. Opt. Soc. Am. **68**, 1651–1658 (1978).
11. N. M. Law, C. D. Mackay, and J. E. Baldwin, "Lucky imaging: high angular resolution imaing in the visible from the ground," Astron. Astrophys. **446**, 739–745 (2006).
12. C. Mackay, J. Baldwin, N. Law, and P. Warner, "High resolution imaging in the visible from the ground without adaptive optics: new techniques and results," Proc. SPIE **5492**, 128–135 (2004).
13. G. W. Carhart and M. A. Vorontsov, "Synthetic imaging: nonadaptive anisoplanatic image correction in atmospheric turbulence," Opt. Lett. **23**, 745–747 (1998).
14. M. A. Vorontsov and Gary W. Carhart, "Anisoplanatic imaging through turbulent media: image recovery by local information fusion from a set of short-exposure images," J. Opt. Soc. Am. A **18**, 1312–1324 (2001).
15. J. W. Goodman, *Introduction to Fourier Optics*, 3rd ed. (Roberts & Company, 2005), Section 6.3.
16. N. Roddier, "Atmospheric wavefront simulation using Zernike polynomials," Opt. Eng. **29**, 1174–1180 (1990).
17. J. W. Goodman, *Introduction to Fourier Optics*, 3rd ed. (Roberts & Company, 2005), Section 6.4.3.
18. Mathematica 6.0, from the test images file: Boat.
19. W. T. Rhodes, "Phase closure and lucky imaging," Appl. Opt. **48**, (this issue).